JOURNAL OF AIRCRAFT
Vol. 41, No. 5, September–October 2004

Dynamic-Stall Control Based on an Optimal Approach

Taisul Ahn,* Chongam Kim,† and Oh-Hyun Rho‡
Seoul National University, Seoul 151-742, Republic of Korea

The present paper investigates methods to control dynamic stall using an optimal approach. Exploiting an unsteady aerodynamic sensitivity analysis based on a direct differentiation method from a two-dimensional unsteady compressible Navier–Stokes solver including a two-equation turbulence model, dynamic-stall control is conducted by minimizing an objective function defined at an instant instead of integrating for a period of time. Unsteady sensitivity derivatives of the objective function are calculated by the sensitivity code, and then optimization is carried out using a linear line search method at every physical time step. Adopting several control parameters such as nose radius, and maximum thickness of airfoil and suction, their effects on the delay or suppression of dynamic stall are examined in detail. Numerous results and comparisons indicate that the present approach yields predictive and more efficient results compared to conventional methods, and suction near the leading edge is essentially more effective than the geometric changes of airfoil in controlling dynamic stall.

Nomenclature

Cp	=	surface-pressure coefficient
$C\mu$	=	suction momentum coefficient
F	=	objective function
M	=	local Mach number
r	=	nose radius of airfoil
t	=	maximum airfoil thickness
α	=	pitching angle
β	=	control variable

Subscripts

max	=	maximum value in the computed flowfield
min	=	minimum value in the computed flowfield
0	=	target value

Introduction

DYNAMIC stall usually refers to unsteady flow separation occurring on aerodynamic bodies, such as airfoils and wings, which undergo a high angle-of-attack unsteady motion. The main reason for dynamic stall is that as an airfoil pitches up vortices started on the leading/tailing edge of the airfoil develop, shed, and subsequently interact with one another on the downstream flowfield. It is the complex fluid dynamic phenomena of practical importance, which can be observed in many aerodynamic applications such as retreating helicopter rotor blades, rapidly maneuvering aircraft, or compressor blades and wind turbines. In most cases, dynamic stall is a primary limiting factor in determining the performance of associated vehicles or structures.[1,2]

Several methods to control dynamic stall have been reported in the literature. One is to employ a leading-edge slat device, which was studied numerically by Tuncer and Sankar[3] using a two-dimensional Navier–Stokes solver for multi-element airfoils. Another is to utilize blowing/suction. Seifert and Pack[4] conducted a dynamic-stall control experiment using blowing slots located at 10 and 70% chord. Sun and Sheikh[5] numerically simulated dynamic-stall control with tangential blowing near the leading edge. Alrefai and Acharya[6] adopted a suction placed at 2% chord and showed that optimal suction speed depends on the definition of the objective function. The third approach is to deform airfoil geometry. Sahin et al.[7] gradually changed the nose radius of the airfoil to delay flow separation. Geissler and Raffel[8] changed airfoil thickness from NACA0012 to NACA0018. Yu et al.[9] used the nose droop of VR-12 airfoil. The rotation angle was located at 25% chord, and the droop angle was 13 deg.

Experiments or numerical simulations confirm that dynamic stall can be alleviated or delayed with suitable control devices, but do not always yield predictive results because control variables were usually prescribed beforehand instead of being changed adaptively depending on the characteristics of flowfield. Thus, the introduction of optimal control approaches into flow analysis is essential in order to find the optimum variation of control variables in a predictive manner. Unlike traditional approaches, they make it possible to carry out feedback dynamic-stall control without any prior knowledge about unsteady flow characteristics.

However, optimal flow control methods developed so far were mainly applied to incompressible low-Reynolds-number flows because the governing equations can be treated more readily compared to the cases of high-Reynolds-number compressible flows. Joslin et al.[10] applied the coupled system of the unsteady incompressible Navier–Stokes equations, an adjoint Navier–Stokes system, and optimality conditions to the problem of boundary-layer instability suppression. Teman et al.[11] applied an optimal feedback control utilizing an adjoint method to low-Reynolds-number turbulent channel flows and obtained a significant reduction in drag. Min and Choi[12] employed a suboptimal feedback control method for the vortex shedding control of a circular cylinder wake flow. Kim et al.[13,14] developed steady and unsteady sensitivity analysis codes of a compressible Navier–Stokes solver with an algebraic turbulence model and applied them to several flow control problems.

The main objective of the present study is to improve the dynamic-stall characteristics of aerodynamic bodies utilizing an optimal control method, which is based on an unsteady sensitivity analysis method for compressible turbulent flows. The unsteady sensitivity analysis code is developed from an unsteady Navier–Stokes solver. To incorporate the effect of turbulence as much as possible without incurring too much computational burden, an advanced two-equation turbulence model is used in flow solver and sensitivity analysis code. Computational cost is then reduced by parallelizing both the flow solver and the sensitivity code on a Linux cluster machine with 32 processors. An objective function for dynamic-stall control is defined by utilizing the local maximum Mach number and the minimum pressure coefficient, which usually occurs near the leading edge of airfoil. It is then minimized at each physical time level by a simple line search method. Using several control parameters such as nose radius and maximum thickness of airfoil and

Presented as Paper 2001-0255 at the 39th Aerospace science Meeting and Exhibit, Reno, NV, 8 January 2001; received 29 April 2003; revision received 28 November 2003; accepted for publication 28 November 2003.

*Graduate Research Assistant, Department of Aerospace Engineering.
†Assistant Professor, Department of Aerospace Engineering; chongam@plaza.snu.ac.kr. Member AIAA.
‡Professor, Department of Aerospace Engineering. Associate Fellow AIAA.

suction, their effects on the delay and/or suppression of dynamic stall are investigated in detail.

Flow Analysis

The steady compressible Navier–Stokes code with two-equation turbulence models developed and validated in Ref. 15 is used as a baseline code for the development of an unsteady flow solver. The two-dimensional unsteady compressible Reynolds-averaged Navier–Stokes equations in generalized coordinates are used in conservation form based on a cell-centered finite volume approach. Roe's flux-difference-splitting scheme is adopted for the spatial discretization of inviscid flux terms, and a monotone upstream centered schemes for conservation laws (MUSCL) approach using a third-order interpolation is used to obtain a higher-order spatial accuracy. Second-order central differencing is used for the viscous flux terms of the residual vector. For temporal discretization, a dual-time-stepping method is employed to obtain second-order accuracy. The pseudotime term is discretized by the Euler implicit method and linearized using flux Jacobian. In the implicit part, Yoon's lower-upper symmetric Gauss–Seidel (LU-SGS) method is used, and van Leer's flux vector splitting with first-order accuracy is adopted for the flux Jacobian. Local time stepping is used for pseudotime integration. Turbulence effects are taken into account by implementing Menter's k–ω shear stress transport model.[16]

Unsteady Sensitivity Analysis

In the application of gradient-based direct optimization method (GBOM), one of the major concerns is the accurate and efficient calculation of sensitivity derivatives of system responses of interest, which are the derivatives of a local maximum Mach number and a minimum surface-pressure coefficient with respect to control variables in the present study.

The method of finite difference approximation is the easiest way to use because it does not require any development of a sensitivity code. However, the accuracy and computational cost of finite difference approach depends critically on the perturbation size of control variables and flow initialization.[17] In addition, as the number of design variables is increased, which would be design and/or flow control cases for complex systems, it is increasingly less efficient compared to a GBOM.

A robust way of computing sensitivity derivatives is to build a sensitivity analysis code, which can be developed by direct-differentiation (DD) methods or adjoint-variable methods. In the present research, DD methods are adopted only for the purpose of computational efficiency because the number of control variables is not large compared to the number of objectives or constraints. The discrete residual vector for the nonlinear aerodynamic analysis of unsteady flow problems with a dual-time-stepping method can be written symbolically at the $(n+1)$th time level as follows:

$$R^{n+1}[Q, X, \beta] + \frac{3Q^{n+1}[\beta] - 4Q^n + Q^{n-1}}{2J\Delta t} = 0 \qquad (1)$$

where Q is the conservative flow vector including turbulence transport terms, X is the grid position vector, β a control variable at the $(n+1)$th time level, R is the residual vector, and J is the flux Jacobian. By directly differentiating Eq. (1) with respect to the control variable β^{n+1} and by implementing the same time-integration approach as the flow solver, the following form can be obtained:

$$\left(\frac{I}{J\Delta\tau} + \left[\frac{\partial R}{\partial Q}\right] + \frac{1.5I}{J\Delta t}\right)\Delta\left(\frac{\mathrm{d}Q}{\mathrm{d}\beta}\right) = -\left(\left(\left[\frac{\partial R}{\partial Q}\right] + \frac{1.5}{J\Delta t}\right) \times \left\{\frac{\mathrm{d}Q}{\mathrm{d}\beta}\right\}^{n+1,s} + \left[\frac{\partial R}{\partial X}\right]\left\{\frac{\mathrm{d}X}{\mathrm{d}\beta}\right\}^{n+1} + \left\{\frac{\partial R}{\partial \beta}\right\}^{n+1}\right) \qquad (2)$$

where s denotes the pseudotime level.

Equation (2) is then solved with the LU-SGS scheme that is also used for the flow solver. To avoid memory overload involving the Jacobian matrices $[\partial R/\partial Q]$ and $[\partial R/\partial X]$ in Eq. (2), the terms $[\partial R/\partial Q]\{\mathrm{d}Q/\mathrm{d}\beta\}$ and $[\partial R/\partial X]\{\mathrm{d}X/\mathrm{d}\beta\}$ are calculated at every iteration without explicitly saving $[\partial R/\partial Q]$ and $[\partial R/\partial X]$ (Ref. 13). When the flow variable sensitivity vector $\{\mathrm{d}Q/\mathrm{d}\beta\}^{n+1}$ is obtained, the total derivative of the unsteady system response of interest F^{n+1} is finally obtained by

$$\left\{\frac{\mathrm{d}F}{\mathrm{d}\beta}\right\}^{n+1} = \left\{\frac{\partial F}{\partial Q}\right\}^T \left\{\frac{\mathrm{d}Q}{\mathrm{d}\beta}\right\}^{n+1} + \left\{\frac{\partial F}{\partial X}\right\}^T \left\{\frac{\mathrm{d}X}{\mathrm{d}\beta}\right\}^{n+1} + \left\{\frac{\partial F}{\partial \beta}\right\}^{n+1} \qquad (3)$$

Boundary conditons for the sensitivity equation (2) are obtained by directly differentiating boundary conditions for the discrete flow equations.

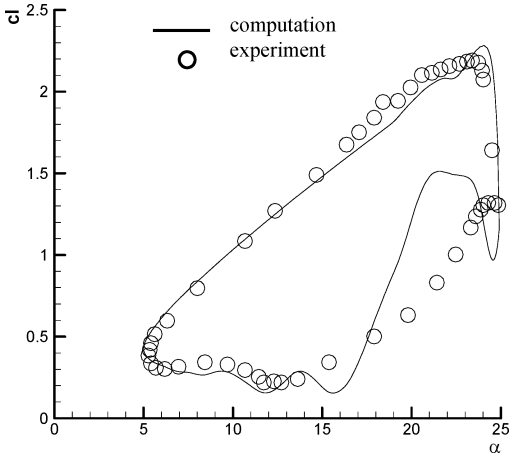

a) History of lift coefficient

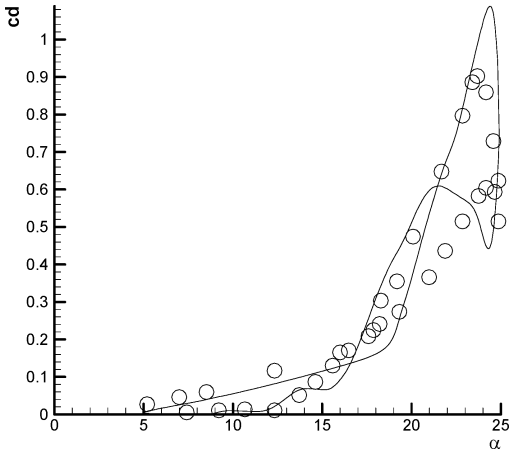

b) History of drag coefficient

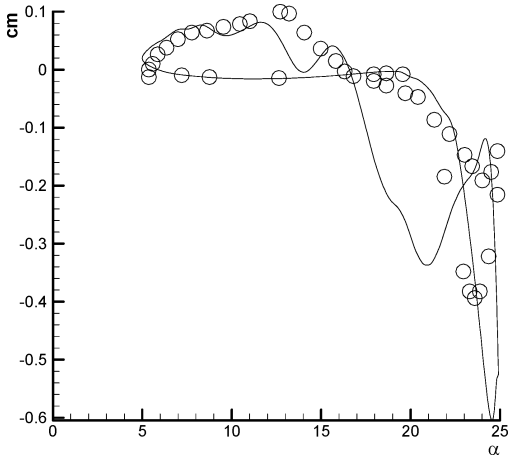

c) History of moment coefficient

Fig. 1 Validation of unsteady flow solver.

Code Validation

To validate the flow solver and sensitivity code, the flowfield of a pitching NACA0012 airfoil is computed at a Mach number of 0.283, a Reynolds number of 3.45×10^6, and a reduced frequency of 0.151. This flow condition corresponds to deep stall and is a typical test case to examine the characteristics of dynamic stall. A 245×127 hyperbolic O-type grid system is used with a wall spacing of 1×10^{-5}. The outer boundary was extended to 15 times the chord length. Preliminary computations indicate it is sufficient to yield grid-converged aerodynamic coefficients. For the pitching motion of the airfoil, grids were moved rigidly. The computations are the results after the third period of pitching motion.

As the validation of the flow solver, an airfoil undergoing pitching motion with respect to its quarter-chord position with the mean angle of attack of 15 deg and the amplitude of 10 deg is chosen. The residual of the unsteady flow solver is reduced to 10^{-6} at each physical time level from the freestream value. Figure 1 shows computed results compared with experimental data.[18] In upstroke motion, the computed aerodynamic coefficients agree fairly well with experimental data, whereas a noticeable discrepancy can be observed in downstroke motion. The main reason for the discrepancy is attributed to the accuracy of turbulence modeling. Although a popular two-equation turbulence modeling is adopted for the simulation of turbulence effects, accurate computations of highly unsteady complex flows such as dynamic-stall phenomenon still require a lot of improvement in this field. Another possibility is transition modeling. The transition point in the present work is located at 3% chord as in experiment. The onset of dynamic stall, that is, separation, is preceded by the formation of a separation bubble. This phenomenon, however, should be simulated more accurately with an improved transition model.[19,20] In spite of these modeling issues, the present results are more acceptable compared to other computations.[19] Also, the present work is mainly focused on the delay or suppress of dynamic stall with an available turbulence modeling, especially on the flow characteristics in up-stroke motion.

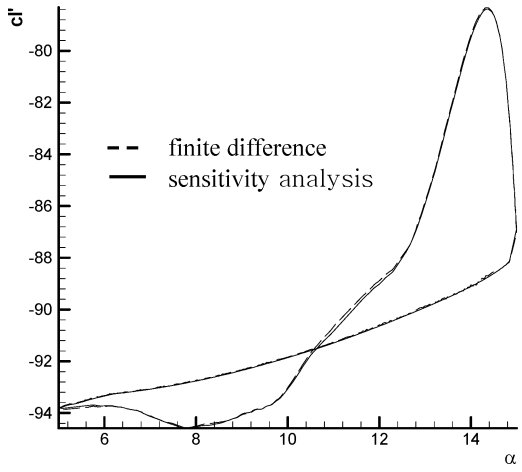

a) Lift-coefficient derivative

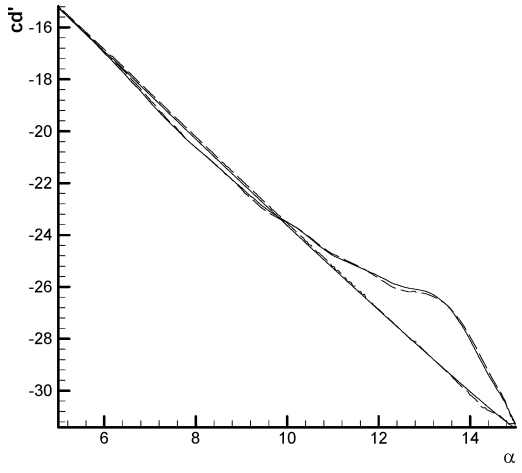

b) Drag-coefficient derivative

Fig. 2 Validation of sensitivity analysis code.

Similar to the validation of the flow solver, a pitching airfoil about its quarter-chord position with a mean angle of attack of 10 deg and amplitude of 5 deg is chosen for the validation of the sensitivity code. Residual at each physical time level is reduced to 10^{-5} from the initial value. The unsteady sensitivity derivative is then compared to the second-order central difference approximation with the step size 1.0×10^{-4} The magnitude of the step size is determined from numerical experiment. To change the airfoil geometry, a Hicks–Henne shape function is used. Figure 2 compares sensitivity derivatives of the lift coefficient $c_l'(=\mathrm{d}c_l/\mathrm{d}\beta)$ and drag coefficient $c_d'(=\mathrm{d}c_d/\mathrm{d}\beta)$. Discrepancies between the results of finite difference method and sensitivity analysis are found to be negligible.

Objective Function

An objective function to control dynamic stall can be formulated by global or local values. First, we can consider an objective function to maximize or minimize the minimum or maximum global values such as the maximum lift coefficient, the minimum moment coefficient, and so forth. Although they are important parameters to examine the characteristics of dynamic stall, this definition imposes tough problems to handle such as memory overhead and computational cost, that is, it needs information on the flowfield and sensitivity of control variable for the entire computational history, which requires a lot of computing time. A more conventional approach to adopt other global aerodynamic coefficients also needs the effects of previous time history because of the time-delay tendency in dynamic stall and the dependency of aerodynamic coefficients on the previous flowfield.

Second, an objective function can exploit local values such as a local Mach number, a surface-pressure coefficient, an adverse pressure gradient, and so forth. It has merits to relieve the burden of memory overhead and computational cost compared to the previous approaches because optimization can be executed at an instantaneous time level. From the viewpoint of computational efficiency, an objective function is defined by the local maximum Mach number or the minimum surface-pressure coefficient at an instantaneous time level instead of adopting a time integral form such as

$$\bar{F} = \int_{T_1}^{T_2} F(t)\,\mathrm{d}t$$

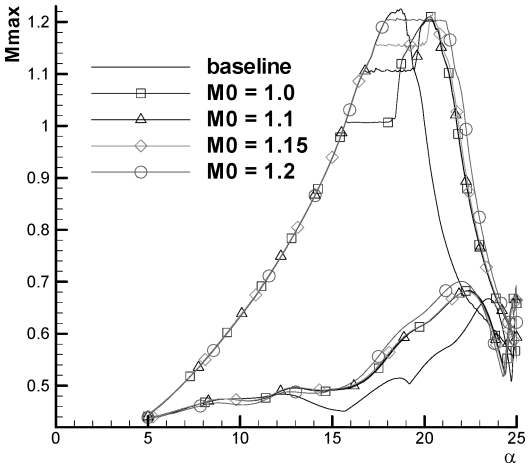

Fig. 3 Local maximum Mach number with nose radius ($F = M_{\max} - M_0$).

Local Maximum Mach Number

Vortex intensity from the initial development to the final shedding can be readily estimated by a local maximum Mach number, as shown in Fig. 3. In this test case, a leading-edge vortex starts to shed as the local maximum Mach number exceeds 1.2. And the onset of dynamic stall also influences upon the pattern of the aerodyanmic coefficients; the slope of lift coefficient changes and drag coefficient sharply increaes. Thus, the local maximum Mach number is a good indicator to examine the developemnt of dynamic stall.

We define an objective function based on the local maximum Mach number as follows:

Minimize

$$F = M_{\max} - M_0 \qquad \text{if} \qquad M_{\max} > M_0 \tag{4}$$

Here, $M_{\max}$ is the local maximum Mach number in flowfield. The definition of Eq. (4) means that control parameters change such that the local maximum Mach number does not exceed M_0. To see the effect of M_0, it is set to 1, 1.1, 1.15, or 1.2 in cases of nose radius or maximum thickness variation. In suction case, M_0 is set to a linear, an exponential, or a sinusoidal function of the angle of attack because the local maximum Mach number increases as suction velocity becomes larger.

Minimum Surface-Pressure Coefficient

In leading-edge separation, the simplest criterion of separation is to check the minimum surface-pressure coefficient. Separation of flows happens when an adverse pressure gradient dominates the kinetic energy of fluid elements. By maintaining the value of the minimum surface-pressure coefficient just above the level of separation, the magnitude of an adverse pressure gradient related to separation can be reduced as the angle of attack increases. In general, the value of the minimum surface-pressure coefficient is about 10 to 13 when the flow begins to separate. Thus, we define an objective function using the minimum surface-pressure coefficient as follows:

Minimize

$$F = c_{p\min} - c_{p0} \qquad \text{if} \qquad c_{p\min} < c_{p0} \tag{5}$$

Here, $Cp_{\min}$ is the minimum surface-pressure coefficient. The definition of Eq. (5) is similar to Eq. (4) in the sense that the minimum surface-pressure coefficient does not exceed Cp_0. Cp_0 is set to 11, 11.5, 12, and 12.5 in cases of nose radius or maximum thickness variation.

Strategy for Dynamic Stall Control

It is assumed that the unsteady objective function F for dynamic-stall control is nonnegative and shows locally a linear behavior with respect to the variation of control input $\{\beta\}$. Thus, $F(\beta + \Delta\beta) \cong F(\beta) + \nabla F \cdot \{\Delta\beta\}$. When the objective function is to be minimized, $\{\Delta\beta\}$ can be determined by $\{\Delta\beta\} = -a\{\nabla F\}$ with a positive number a. Because $\{\Delta\beta\}$ will drive $F(\beta + \Delta\beta)$ to zero at the optimum position, we can eventually obtain $a = F(\beta)/|\nabla F|^2$, and thus $\{\Delta\beta\} = -F/|\nabla F|^2\{\nabla F\}$. If the assumption is not valid or does not yield satisfactory results, other line search methods such as a quadratic line search method or more sophisticated optimization algorithms for multidimensional problems can be used at the expense of computational cost. In the present study, however, the simple line search method is good enough to provide satisfactory results. Thus, we employ the following procedure to minimize the unsteady objective function F:

1) Obtain F^{n+1} for $\{\beta\} = \{\beta\}^n$ by the flow solver.

2) Obtain $\{\nabla F\}^{n+1}$ for $\{\beta\} = \{\beta\}^n$ by the sensitivity code.

3) Obtain $\{\beta\}^{n+1}$ as $\{\beta\}^{n+1} = \{\beta\}^n + \{\Delta\beta\}$ with $\{\Delta\beta\} = -F/|\nabla F|^2\{\nabla F\}$.

4) Update F^{n+1} for $\{\beta\} = \{\beta\}^{n+1}$ by the flow solver.

5) Go to the next time level (1).

Control Variables

To control dynamic stall, many concepts were proposed, as mentioned earlier. One of them is to add energy to boundary layer. For example, pressure field can be substantially affected by changing airfoil geometry such as nose radius and maximum thickness. Another is to take away low-energy fluids through suction. Flowfield can maintain a stabilized state by absorbing disturbances on the airfoil. Based on these concepts, three control parameters are chosen in this study; the nose radius r, the maximum airfoil thickness t, and the suction momentum coefficient $C\mu$.

For the change of the nose radius, the airfoil geometry up to 40% of chord length from the leading edge varies as a linear combination of NACA0012 and NACA0018 airfoils while other part is fixed as NACA0012 airfoil. NACA0012 airfoil has the nose radius of 0.016 and the upper limit of r is 0.036, which is the radius of NACA0018 airfoil. In the case of the maximum airfoil thickness, the airfoil geometry is varied linearly from NACA0012 to NACA0018 according to the variation of t.

The third control parameter used in this analysis is the suction momentum coefficient, which is defined as $C_\mu = 2(h/c)(M_j/M_\infty)^2$. Here, h is the slot width, c the chord length, and M_j the mean slot inlet Mach number that is constrained to be less than 0.3. To decide the location of slots, simple tests are conducted with constant suction momentum coefficient. Based on these results, suction slots are located from 7 to 12% chord. In actual implementation, velocity boundary conditions on the wall are explicitly specified from suction momentum coefficients. Because the sensitivity derivatives of an objective function with respect to the suction velocity of each slot are of the same order, suction velocity at each slot is assumed to be the same for the sake of computational efficiency.

Control Results

In all test cases, flow conditions are the same as in the validation of the flow solver ($M_\infty = 0.283$, $Re = 3.45 \times 10^6$). In a control procedure, convergence criteria for the flow solver and the sensitivity code are 10^{-5} from a freestream value and 10^{-4} from an initial value, respectively. Optimization technique is then applied during up-stroke motion. In downstroke motion, control parameters are prescribed such that r and t vary linearly and $C\mu$ sinusoidally from the final to the initial state.

Nose Radius

Local Maximum Mach Number

Figures 3 and 4 show the variation of the local maximum Mach number before and after the control and the history of the control parameter r, respectively. According to the magnitude of M_0, the control is activated at different angles of attack. All control cases are well maintained at M_0 during the optimization process. Except for the case of $M_0 = 1.2$, after the control variable reaches its upper limit the local maximum Mach number somewhat increases until the flows are finally separated. In the case of $M_0 = 1.2$, the maximum nose radius 0.0295 is smaller than the upper limit of r. Optimization is not conducted because the local maximum Mach number is less than 1.2 until the flows on the airfoil are finally separated.

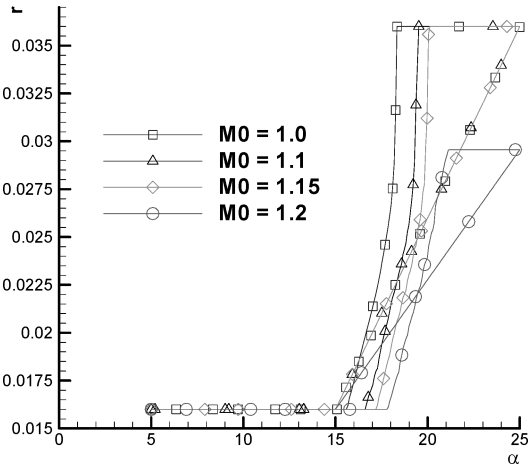

Fig. 4 Variation of nose radius ($F = M_{\max} - M_0$).

Table 1 Features of aerodynamic coefficients with r and M_{max}

Cases	Max. c_l	Lift stall angle, deg	Max. c_d	Drag-divergent angle, deg	Min. c_m	Moment stall angle, deg
Baseline	2.28	24.0	1.089	18.6	−0.604	19.3
$M_0 = 1.0$	2.28	24.5	1.050	20.2	−0.675	21.3
$M_0 = 1.1$	2.29	24.5	1.049	20.1	−0.676	21.3
$M_0 = 1.15$	2.27	24.5	1.044	20.5	−0.668	21.3
$M_0 = 1.2$	2.23	24.6	1.036	21.0	−0.656	21.1

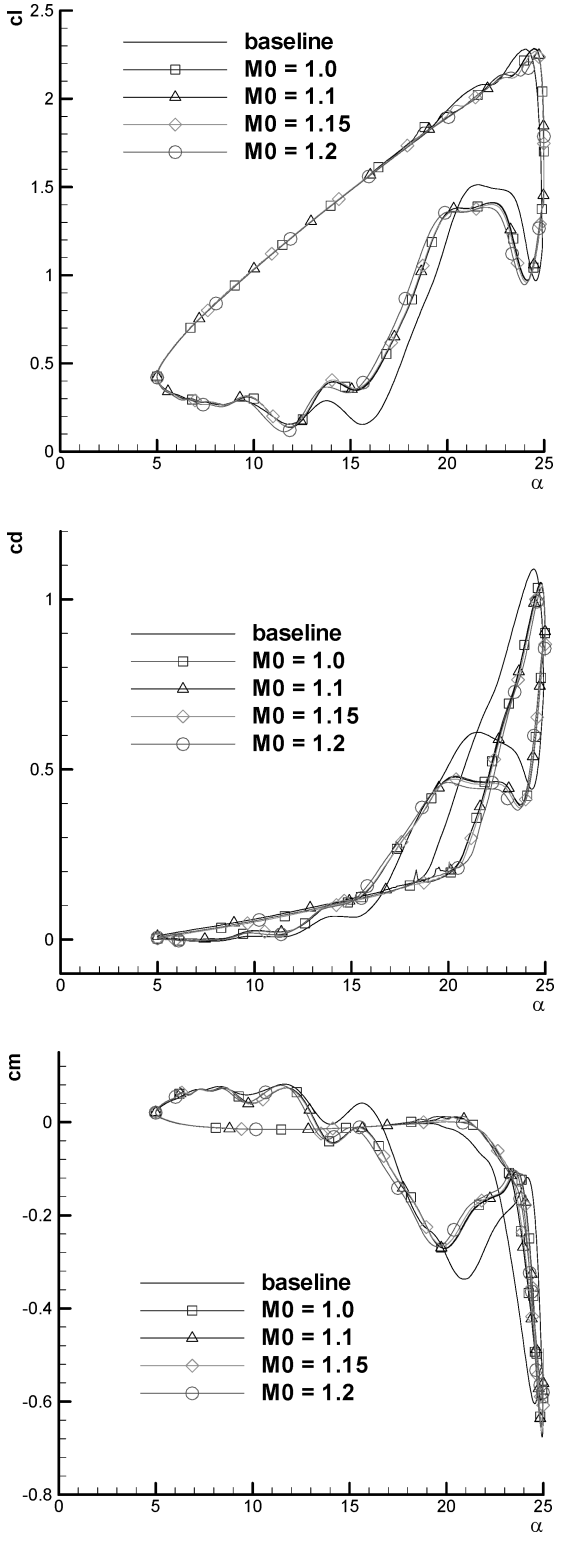

Fig. 5 Aerodynamic coefficients before and after control with nose radius ($F = M_{max} - M_0$).

Comparison of aerodynamic coefficients is presented in Fig. 5, and the summary of computed results is given in Table 1. The angle of attack for the maximum lift coefficient is similar to the value of the baseline airfoil except for the case of $M_0 = 1.2$, which is slightly decreased. All control cases delay the lift stall about 0.5 deg. The maximum drag coefficient is reduced in proportional to the value of M_0. Drag divergence is delayed from 1.5 to 2.4 deg, and the moment stall angle is also delayed about 2 deg. However, the minimum pitching-moment coefficient is increased compared to the baseline value.

Minimum Surface-Pressure Coefficient

Overall effects using the minimum surface-pressure coefficient are similar to the case of the local maximum Mach number. Thus, similar control results such as the history of control variable or the minimum surface-pressure coefficient and the comparison of aerodynamic coefficients are omitted in this paper.

The distributions of instantaneous surface-pressure coefficient during up-stroke motion are shown in Fig. 6. As the angle of attack increases, the first suction peak eventually decreases, and a point, which changes the sign of the second derivative value of surface-pressure coefficient, appears when vortex starts to separate from the leading edge. Flat region and the second peak value, which represent separated flow region and the location of vortex core on the airfoil, develop and grow as vortex sheds along the upper surface of airfoil. As a result, the maximum lift occurs and then sharply collapses as vortex passes between the quarter-chord and the midchord length. In the present study, the maximum lift coefficient appears when vortex passes through the location of a half-chord length. When an instantaneous angle of attack becomes 24 deg, we can see that the second peak value of the baseline airfoil locates at a half-chord length, that is, lift stall occurs, but in the controlled case the peak value is located ahead of a half-chord length position, indicating that lift still increases and stall is delayed.

Maximum Airfoil Thickness

Local Maximum Mach Number

Figure 7 shows the history of the control parameter t. Similar to the case of nose radius, control ended at $t = 0.172$, and it does not reach the upper limit in $M_0 = 1.2$. From Figs. 3 and 8, it can be seen that the local maximum Mach number is more effective in thickness control than nose radius control. This is because of the change of flow separation pattern. In nose radius control, separation starts from the leading edge, whereas the opposite trend can be observed in thickness control. Thus, the flow in the leading-edge region can be kept attached to higher incidence angle. Similar to the case of nose radius control, the local maximum Mach number has the highest value around $M_0 = 1.2$.

The behavior of aerodynamic coefficients is presented in Fig. 9. The result with $M_0 = 1.15$ is not presented because it is similar to that of $M_0 = 1.1$. Table 2 summarizes the effect of thickness control. In all control cases, the peak values of the maximum lift coefficients are smeared. This is a typical pattern that can be seen in trailing-edge stall of Fig. 10. Flows are separated from the trailing edge because the airfoil becomes thicker than the baseline airfoil. During downstroke motion, lift remains higher compared to the uncontrolled case because the flow reattaches earlier. The maximum drag is also considerably reduced by about 27%, compared to the case of the baseline airfoil when M_0 equals to 1.15. In addition,

Table 2 Features of aerodynamic coefficients with t ($M_{\max}$ or $Cp_{\min}$)

Cases	Max. c_l	Lift stall angle, deg	Max. c_d	Drag-divergent angle, deg	Min. c_m	Moment stall angle, deg
Baseline	2.28	24.0	1.089	18.6	−0.604	19.3
$M_0 = 1.0$	2.01	24.2	0.837	24.4	−0.495	24.3
$M_0 = 1.1$	2.00	23.0 ∼ 24.0	0.846	24.4	−0.495	24.2
$M_0 = 1.15$	1.99	23.4 ∼ 23.8	0.796	24.1	−0.421	23.7
$M_0 = 1.2$	2.04	25.0	0.922	23.3	−0.504	21.3
$Cp_0 = 12.5$	2.34	24.7	1.136	21.8	−0.658	20.5

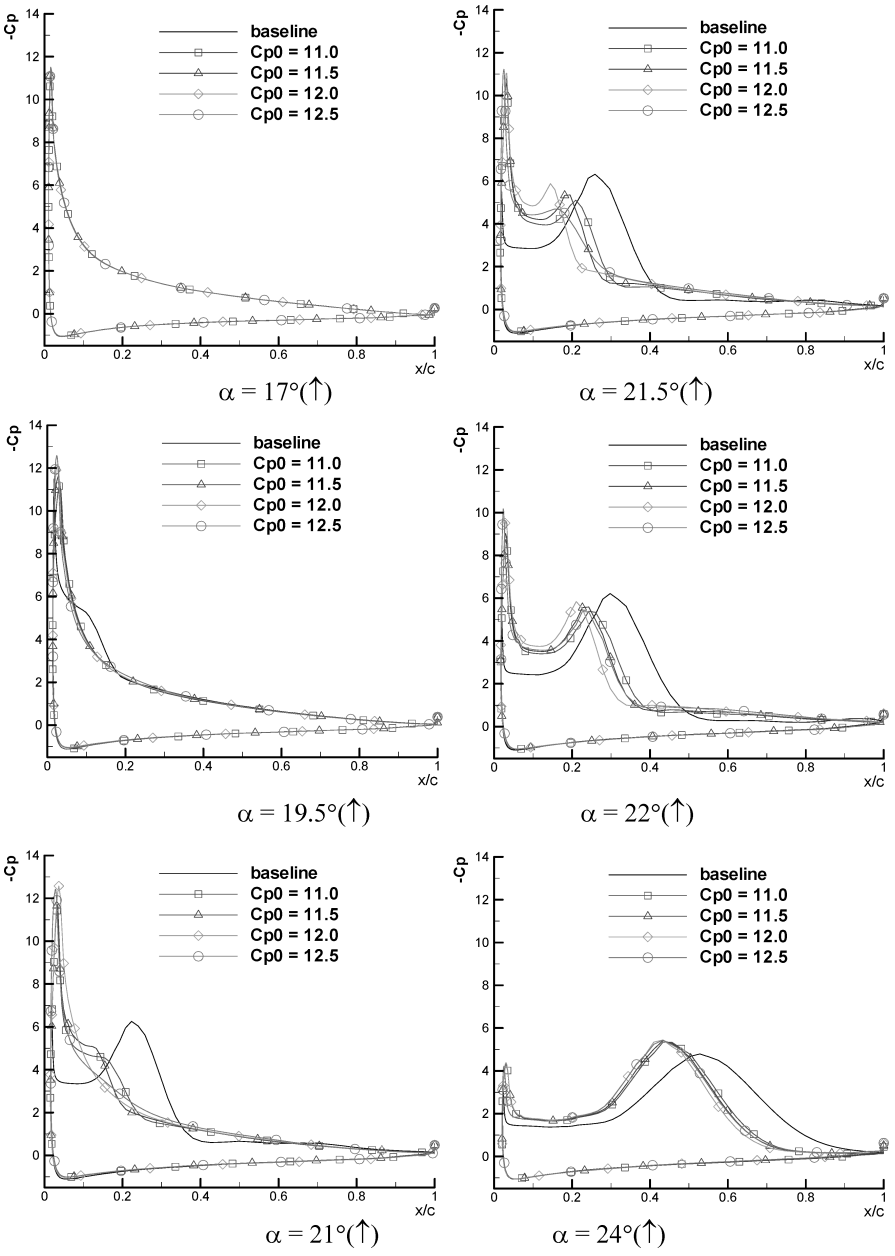

Fig. 6 Surface-pressure distributions before and after control with nose radius ($F = Cp_{\min} - Cp_0$).

the drag-divergence angle keeps a higher value by about 5 deg. As the same time, the intensity of the minimum pitching moment is weakened by 17 to 30%, and the moment stall angle is delayed by 2 to 5 deg. During downstroke motion, the pitching moment recovers more rapidly than the baseline airfoil.

Minimum Surface-Pressure Coefficient

General trend is similar to the case of the local maximum Mach number except for $Cp_0 = 12.5$. In control cases with maximum thickness, separation generally starts from the trailing edge and propagates to the leading edge but, in the case of $Cp_0 = 12.5$, flows separate at the middle chord of airfoil and propagate to the leading edge. As a result, flows on the leading edge are not attached at higher angle of attack, which yields unfavorable behaviors in stall delay. Aerodynamic coefficients are presented in Fig. 9 and summarized in the next section. Results are similar to the nose radius control; lift and moment stall were delayed, but the pitching-moment characteristic became deteriorated.

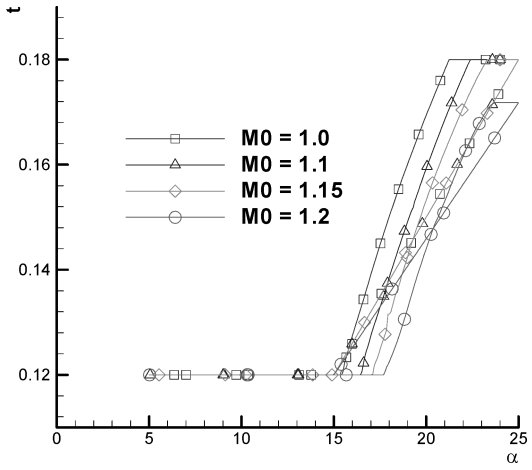

Fig. 7 Variation of maximum airfoil thickness ($F = M_{\max} - M_0$).

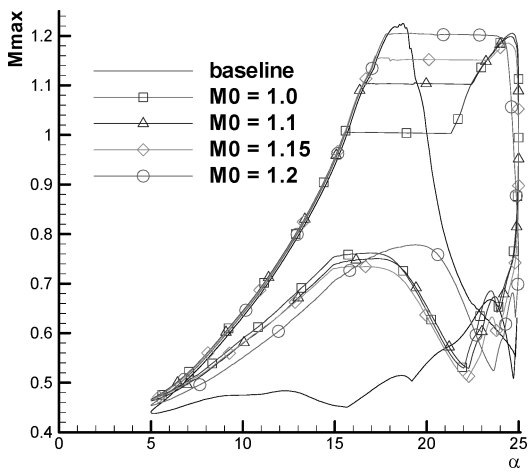

Fig. 8 Local maximum Mach number with maximum airfoil thickness ($F = M_{\max} - M_0$).

Instantaneous surface-pressure coefficient distributions and vortex shedding pattern in Fig. 11 show this behavior more clearly. Except for the $Cp_0 = 12.5$ case, all cases do not show second peak value until about 25 deg, and the first peak value is larger than the second one, which prevents the pitching moment from being a large negative value.

Suction-Momentum Coefficient

In this case, control by either the local maximum Mach number or the minimum surface-pressure coefficient does not yield any noticeable difference. Thus, only the local maximum Mach number is used as an objective function. To examine the accuracy and efficiency of the current approach, mean suction with sensitivity analysis is compared to the results of prescribed control with constant or sinusoidal suction.

The local maximum Mach number tends to increase in proportion to the angle of attack because the disturbances of flowfields are removed with suction. Thus the behavior of M_0 is modeled as a linear, a sinusoidal, or an exponential function to find an effective objective function. Figure 12 shows the history of the control parameter C_μ. When M_0 becomes a linear function, C_μ reaches its upper limit 0.112 at about 21 deg. In other cases, the maximum value of C_μ is reduced to 0.0785 and 0.086, respectively, at the end of upstroke motion, which shows the highly nonlinear behavior of dynamic stall.

During downstroke motion, however, the control variable in all cases has to vary sinusoidally from the upper limit, not from the maximum value, to prevent flow separation, which exhibits a kind of strong hysteresis phenomenon in dynamic stall. It also suggests

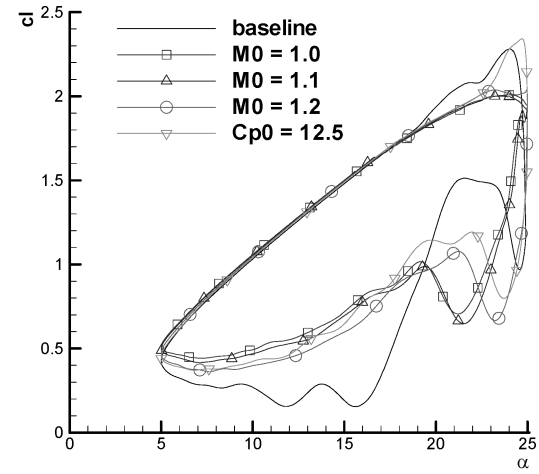

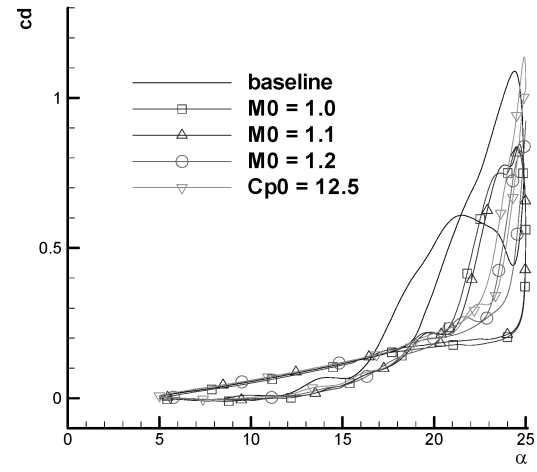

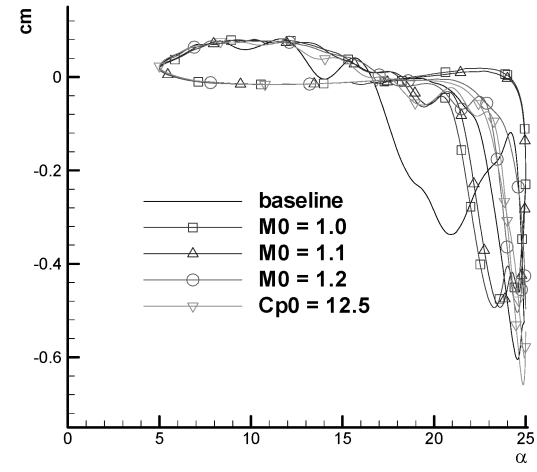

Fig. 9 Aerodynamic coefficients before and after control with maximum thickness ($F = M_{\max} - M_0$ and $Cp_{\min} - Cp_0$).

again that the accurate flow analysis of separated flows in downstroke motion is essential for the complete control of dynamic stall. As seen from the variation of aerodynamic coefficients in Fig. 13, dynamic stall is suppressed completely in all control cases.

Although the range of C_μ is still too high to be practical, it also shows that C_μ can be substantially reduced in a predictive and efficient manner by adopting the current optimal approach. To validate this more quantitatively, prescribed control with constant or sine suction is compared to optimal flow control. In the case of constant

suction, the suction value takes the average value obtained in the optimal control case when M_0 is a linear function. In the case of sine suction, downstroke suction used in the optimal control case is applied symmetrically to up-stroke suction. Computed results indicate that sine suction also suppresses dynamic stall completely. In case of constant suction, lift and moment stall are delayed, and the maximum lift is increased, but the negative maximum pitching moment is increased. Here we summarize the suction efficiency of both the prescribed and optimized control. In the prescribed control with a constant suction, the sum of C_μ is 1.3573 and with a suction of sine function is 1.6856. In the optimized suction with a linear M_0, it is 1.3573, with a sinusoidal M_0 is 1.0557, and with a exponential M_0 is 1.0404. The prescribed control with a sine function requires the largest energy, and the optimized control with a exponential function needs the smallest energy, which confirms the predictive and efficient control of the current optimal approach.

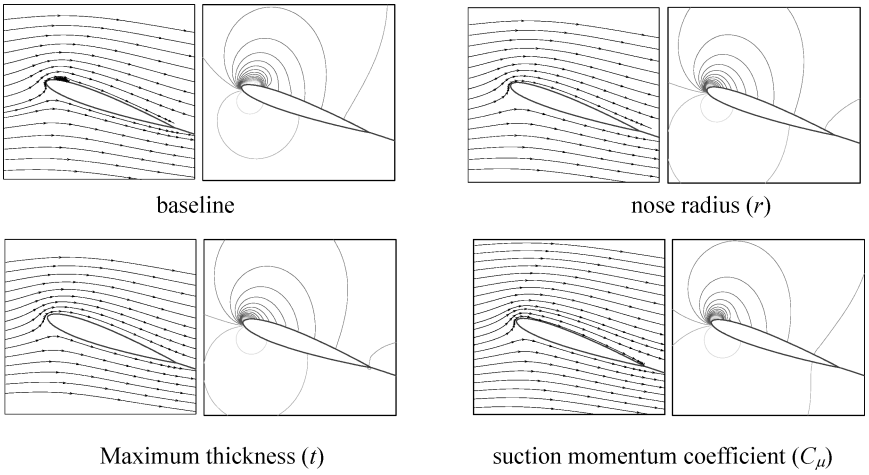

a) Streamlines and pressure contours at $\alpha = 19.60$ deg (↑)

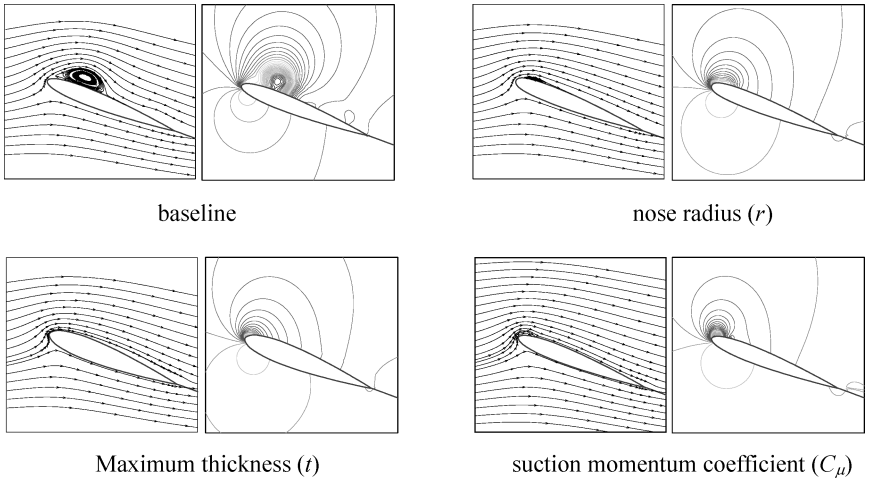

b) Streamlines and pressure contours at $\alpha = 21.52$ deg (↑)

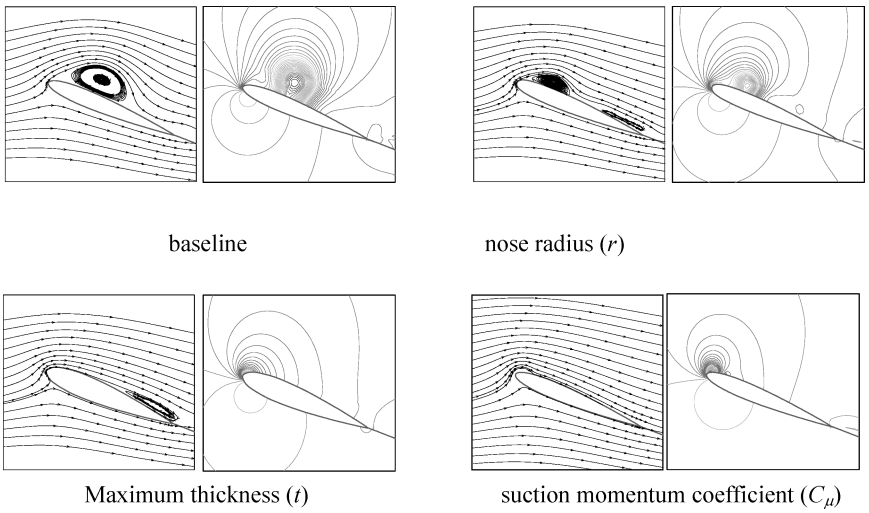

c) Streamlines and pressure contours at $\alpha = 22.60$ deg (↑)

Fig. 10 Instantaneous streamlines and pressure contours.

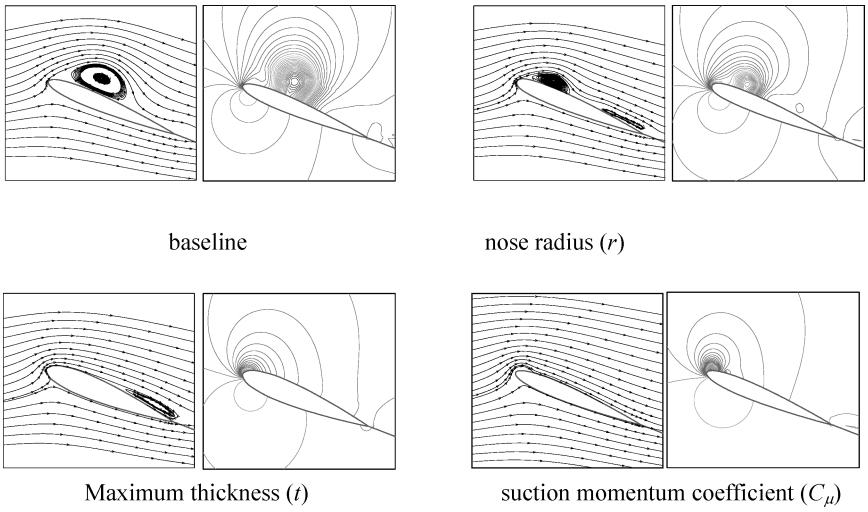

a) Streamlines and pressure contours at $\alpha = 24.31$ deg (↑)

Fig. 10 Instantaneous streamlines and pressure contours (continued).

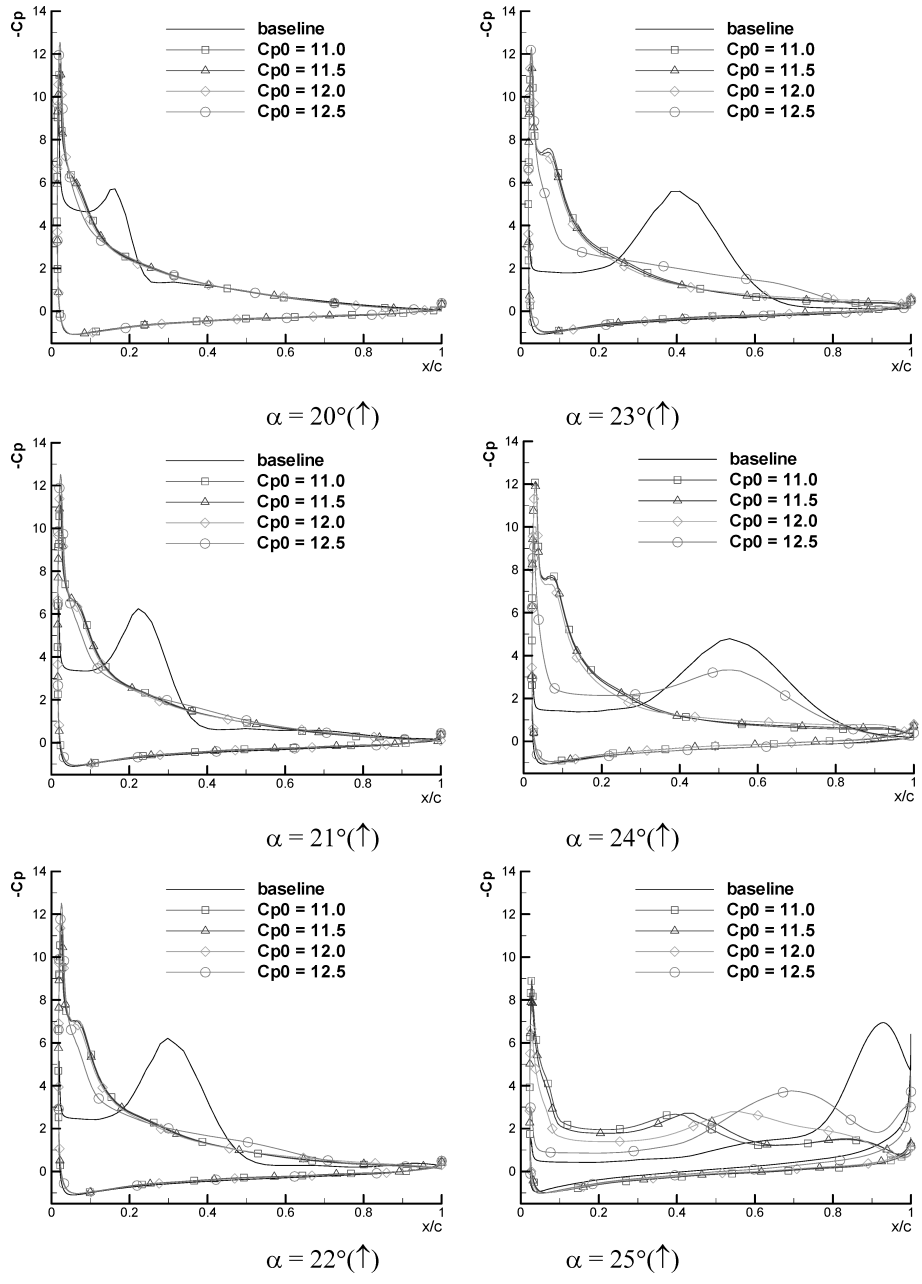

Fig. 11 Surface-pressure distributions before and after control with maximum thickness ($F = Cp_{\min} - Cp_0$).

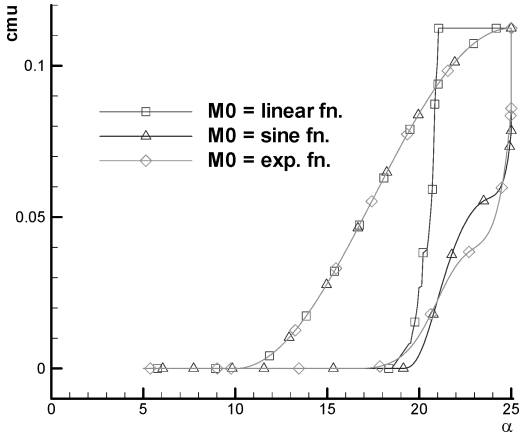

Fig. 12 Variation of suction momentum coefficient.

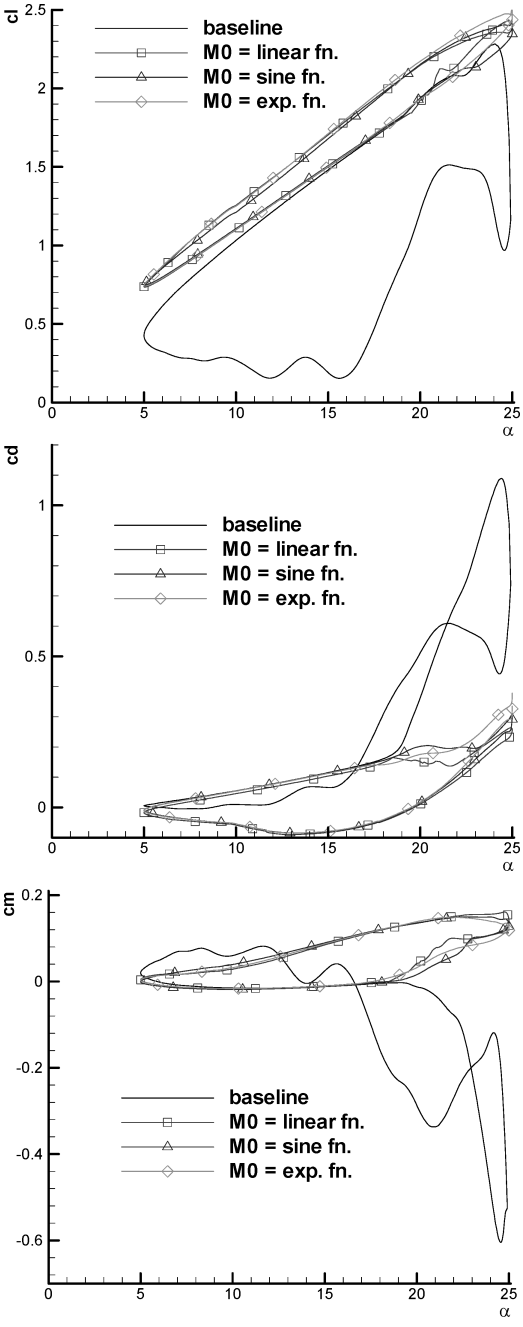

Fig. 13 Aerodynamic coefficients before and after control with suction-momentum coefficient.

Comparison of Control Cases

Except for the case of $Cp_0 = 12.5$ with the maximum thickness, the influence of the objective function is not substantial; lift and moment stall are delayed in the case of nose radius. Lift stall is smeared, and the behavior of moment stall is more improved in the control of the maximum thickness. In the case of $Cp_0 = 12.5$ with the maximum thickness, the results are similar to the nose radius control.

Airfoil geometric change by means of nose radius or the maximum thickness control turns out to be less effective than suction. This is consistent with the reported result that deep dynamic stall is relatively independent of airfoil shape, Reynolds number, cross-flow effects, or the type of airfoil motion.[1] Although many control concepts were introduced and successful results were obtained in previous researches, these approaches require detailed analyses and parametric studies in order to determine the appropriate variation of control variables. In this respect, the current approach, compared to prescribed control, shows the capability of dynamic stall control in a predictive and efficient way.

Figure 10 compares various instantaneous flowfield patterns and pressure distributions during up-stroke motion when the objective function uses the local maximum Mach number. In Fig. 10a, the flow around the baseline airfoil starts to separate near the leading edge, while the flows of the three control cases remain attached to airfoil surface. In Fig. 10b, the baseline flow shows the formation and shedding of leading-edge vortex on suction surface. In case of nose radius control, the flow begins to separate near the leading edge, and a vortex starts to form. However, in case of thickness and suction control flows are still attached on airfoil surface and a vortex is just growing up. In Fig. 10c, the flow of suction surface over the baseline airfoil is dominated by a strong dynamic-stall vortex. Separation region with nose radius control is much smaller, although vortex shedding can be observed. For thickness control, the flow near the leading edge is still attached, and vortex shedding is not observed, but flow separation near the trailing edge can be seen. In the case of suction control, the flow remains attached on the entire upper surface, and vortex shedding is not shown, but the magnitude of suction momentum coefficient needs to be improved further in order to be more practical. Figure 10d shows the flow pattern in the maximum pitch-up position. Flows over the baseline airfoil and with radius control are fully separated over the entire suction surface and in the state of deep stall, although the relative size of vortices is somewhat different. In the case of thickness control, the flow still remains attached near the leading edge, but sizable vortex shedding can be observed near the trailing edge. On the other hand, the flow with suction control is similar to the case of Fig. 10c.

Conclusions

A novel dynamic-stall control concept using an optimal approach is presented and validated. The unsteady derivative of the objective function is obtained by a direct differentiation method, and a simple line search method is used to determine the step size of control variable. The objective function is defined by a local value to reflect the time-delay characteristic of dynamic stall. The effects of geometric change of airfoil or of suction on dynamic stall are investigated by adopting several control parameters, such as nose radius, maximum thickness, or suction-momentum coefficient.

Although the change of airfoil shape brings enhanced results in terms of dynamic-stall onset, drag reduction, flow reattachment in downstroke motion, it is still incomplete in a sense that it does not suppress deep dynamic stall. Suction near the leading edge shows substantial improvement in delaying or suppressing dynamic stall, but suction-momentum coefficient has to improve further in order to be more practical.

The efficiency of the current approach is confirmed by comparing the results of the optimized control with the prescribed control; the prescribed control spends more energy than the optimized control in determining a history of a control variable and, in addition, requires a parametric study. Although the present study focuses on up-stroke motion, the current optimization process can be extended

to downstroke motion with the refined flow analysis of turbulence effects.

Acknowledgments

The authors acknowledge the financial support provided by the Korea Science and Engineering Foundation (Grant R01-2002-000-00329-0) and by the Brain Korea 21 Project.

References

[1]McCroskey, W. J., McAlister, K. W., Carr, L. W., Pucci, S. L., Lambert, O., and Indergrand, R. F., "Dynamic stall on Advanced Airfoil Sections," *Journal of the American Helicopter Society*, Vol. 26, No. 3, 1981, pp. 40–50.

[2]Carr, L. W., "Progress in Analysis and Prediction of Dynamic Stall," *Journal of Aircraft*, Vol. 25, No. 1, 1988, pp. 6–17.

[3]Tuncer, I., and Sankár, L. N., "Unsteady Aerodynamic Characteristics of a Dual-Element Airfoil," *Journal of Aircraft*, Vol. 31, No. 3, 1994, pp. 531–537.

[4]Seifert, A., and Pack, L. G., "Oscillation Control of Separation at High Reynolds Numbers," *AIAA Journal*, Vol. 37, No. 9, 1999, pp. 1062–1071.

[5]Sun, M., and Sheikh, S. R., "Dynamic Stall Suppression on an Oscillating Airfoil by Steady and Unsteady Tangential Blowing," *Aerospace Science and Technology*, Vol. 3, No. 6, 1999, pp. 355–366.

[6]Alrefai, M., and Acharya, M., "Controlled Leading-Edge Suction for Management of Unsteady Separation over Pitching Airfoils," *AIAA Journal*, Vol. 34, No. 11, 1996, pp. 2327–2336.

[7]Sahin, H., Sankar, L. N., Chandrasekhara, and Tung, C., "Dynamic Stall Alleviation Using a Deformable Leading Edge Concept—A Numerical Study," *Journal of Aircraft*, Vol. 40, No. 1, 2003, pp. 77–85.

[8]Geissler, W., and Raffel, M., "Dynamic Stall Control by Airfoil Deformation," *19th European Rotorcraft Conference*, Vol. 1, 1993, C2-1–13.

[9]Yu, Y. H., Lee, S., McAlister, K. W., Tung, C., and Wang, C. M., "Dynamic Stall Control for Advanced Rotorcraft Application," *AIAA Journal*, Vol. 33, No. 2, 1995, pp. 289–295.

[10]Joslin, R. D., Gunzburger, M. D., Nicolaids, R. A., Erlebacher, G., and Hussaini, M. Y., "A Self-Contained, Automated Methodology for Optimal Flow Control Validated for Transition Delay," NACA CR 198215, ICASE Rept. 95-64, Sept. 1995.

[11]Teman, R., Bewley, T., and Moin, P., "Control of Turbulent Flows," *Proceedings of the 18th IFIP TC7 Conference on System Modeling and Optimization*, edited by M. P. Polis, E. L. Dontchev, P. Kall, I. Lasiecka, and A. W. Olbert, Chapman and Hall, 1997.

[12]Min, C., and Choi, H, "Suboptimal Feedback Control of Vortex Shedding at Low Reynolds Numbers," *Journal of Fluid Mechanics*, Vol. 401, Dec. 1999, pp. 123–156.

[13]Kim, H. J., Kim, C., and Rho, O. H., "Flow Control Using Unsteady Aerodynamic Sensitivity Analysis," AIAA Paper 2000-0515, Jan. 2000.

[14]Kim, H. J., Kim, C., Rho, O. H., and Lee, K., "Aerodynamic Sensitivity Analysis for Navier-Stokes Equations," AIAA Paper 99-0402, Jan. 1999.

[15]Kim, C. S., Kim, C., and Rho, O. H., "Parallel Computations of High Lift Airfoil Flows Using Two-Equation Turbulence Models," *AIAA Journal*, Vol. 38, No. 8, 2000, pp. 1360–1368.

[16]Menter, F. R., "Two-Equation Eddy-Viscosity Turbulence Models for Engineering Applications," *AIAA Journal*, Vol. 32, No. 8, 1994, pp. 1598–1605.

[17]Eyi, S., and Lee, K. D., "Effect of Sensitivity Calculation on Navier–Stokes Design Optimization," AIAA Paper 94-0060, Jan. 1994.

[18]McAlister, K. W., Pucci, S. L., McCroskey, W. L., and Carr, L. W., "An Experimental Study of Dynamic Stall in Advanced Airfoil Sections, Vol. 2, Pressure and Force Data," NASA TM 84245, Sept. 1982.

[19]Wu, J. C., Huff, D. L., and Sankar, L. N., "Evaluation of Three Turbulence Models in Static Air Loads and Dynamic Stall Predictions," *Journal of Aircraft*, Vol. 27, No. 4, 1990, pp. 382–384.

[20]Ekaterinaris, J. A., and Platzer, M. F., "Computational Prediction of Airfoil Dynamic Stall," *Progress in Aerospace Sciences*, Vol. 33, April 1998, pp. 759–846.